

# 1 Impact of implementation choices on quantitative predictions of 2 cell-based computational models

3 Jochen Kursawe<sup>1,\*</sup>, Ruth E. Baker<sup>1</sup>, Alexander G. Fletcher<sup>2,3</sup>

4 <sup>1</sup> Mathematical Institute, University of Oxford, Andrew Wiles Building, Radcliffe Observatory  
5 Quarter, Woodstock Road, Oxford, OX2 6GG, UK

6 <sup>2</sup> School of Mathematics and Statistics, University of Sheffield, Hicks Building, Hounsfield  
7 Road, Sheffield, S3 7RH, UK

8 <sup>3</sup> Bateson Centre, University of Sheffield, Sheffield, S10 2TN, UK

9 \* E-mail: kursawe@maths.ox.ac.uk

## 10 Abstract

11 ‘Cell-based’ models provide a powerful computational tool for studying the mechanisms underlying  
12 the growth and dynamics of biological tissues in health and disease. An increasing amount of  
13 quantitative data with cellular resolution has paved the way for the quantitative parameterisation  
14 and validation of such models. However, the numerical implementation of cell-based models  
15 remains challenging, and little work has been done to understand to what extent implementation  
16 choices may influence model predictions. Here, we consider the numerical implementation of a  
17 popular class of cell-based models called vertex models, used extensively to simulate epithelial  
18 tissues. In two-dimensional vertex models, a tissue is approximated as a tessellation of polygons  
19 and the vertices of these polygons move due to mechanical forces originating from the cells. We  
20 analyse how the model predictions may be affected by implementation-specific parameters, such  
21 as the size of the numerical time step. We find that vertex positions and summary statistics  
22 are sensitive to multiple implementation parameters. For example, the predicted tissue size decreases  
23 with decreasing cell cycle durations, and cell rearrangement may be suppressed by large  
24 time steps. These findings are counter-intuitive and illustrate that model predictions need to be  
25 thoroughly analysed and implementation details carefully considered when applying cell-based  
26 computational models in a quantitative setting.

## 27 1 Introduction

28 Computational modelling is increasingly used in conjunction with experimental studies to un-  
29 derstand the self-organisation of biological tissues [1,2]. Popular computational models include  
30 ‘cell-based’ models that simulate tissue behaviour with cellular resolution. Such models natu-  
31 rally capture stochastic effects and heterogeneity when only few cells are present and can be  
32 used to explore tissue behaviour when complex assumptions on the cellular scale prevent us  
33 from deriving continuum approximations on the tissue scale. The applications of cell-based  
34 models range from embryonic development [3–7], to wound healing [8] and tumour growth [9].  
35 However, the numerical solution of cell-based models remains challenging since multi-scale im-  
36 plementations of such models, coupling processes at the subcellular, cellular, and tissue scale,  
37 may suffer from numerical instabilities [10,11] and such models may include parameters that  
38 have no direct physical correlate. These issues are of growing importance as cell-based models  
39 become used in an increasingly quantitative way [12–14]. Thus, we need to be aware of any  
40 impacts that numerical implementation choices may have on model predictions.

41 Here, we analyse a well-established class of cell-based model, the vertex model [15], to  
42 understand to what extent implementation choices may affect model predictions. Vertex models  
43 were originally developed to study inorganic structures, such as foams [16] and grain boundaries  
44 [17,18], where surface tension and pressure drive dynamics. They have since been modified  
45 to study epithelial tissues [19–22], one of the major tissue types in animals. Epithelia form  
46 polarized sheets of cells with distinct apical (‘top’) and basal (‘bottom’) surfaces, with tight  
47 lateral attachments nearer their apical surface. The growth and dynamics of such sheets play a  
48 central role in morphogenesis and wound healing, as well as in disease; for example, over 80% of  
49 cancers originate in epithelia [23]. In two-dimensional vertex models, epithelial cell sheets are  
50 approximated by tessellations of polygons representing cell apical surfaces, and vertices (where  
51 three or more cells meet) move in response to forces due to growth, interfacial tension and  
52 hydrostatic pressure within each cell (figure 1A-C). Vertex models typically include cell growth  
53 and proliferation. In addition, cells exchange neighbours through so-called T1 transitions (figure  
54 1D) whenever the length of a cell-cell interface falls below a threshold, and any triangular cell  
55 whose area falls below a threshold is removed by a so-called T2 transition (figure 1E).

56 Vertex models have been used to study a variety of processes in epithelial tissues [3,5,6,

57 24–37]. A common approach in such studies is to consider forces on vertices arising as a result  
58 of minimizing the total stored energy in the tissue. The functional form for this total stored  
59 energy varies between applications, but is typically chosen to reflect the effect of the force-  
60 generating molecules which localise at or near the apical surface. This energy function is then  
61 used either to derive forces that feed into a deterministic equation of motion for each vertex,  
62 which must be integrated over time [4, 27, 38], or else minimized directly assuming the tissue  
63 to be in quasistatic mechanical equilibrium at all times [3, 24]. A third approach is to apply a  
64 Monte Carlo stochastic simulation to find energy minima [39, 40].

65 Previous theoretical analyses of vertex models have elucidated ground state configura-  
66 tions [41], inferred bulk material properties [42–44], and introduced ways to superimpose finite-  
67 element schemes for diffusing signals with the model geometry [45]. In other work, vertex  
68 models have been compared to lattice-based cellular Potts models and other cell-based mod-  
69 elling frameworks [46, 47].

70 In the case of vertex models of grain-boundaries, the authors of [18] propose an adaptive  
71 time stepping algorithm to accurately resolve vertex rearrangements without the need of ad-  
72 hoc rearrangement thresholds and provide a numerical analysis of the simulation algorithm.  
73 However, vertex models in that context only consider energy terms linear in each grain-grain (or  
74 cell-cell) interface length, whereas energies in biophysical models typically depend non-linearly  
75 on cell areas and perimeters.

76 Importantly, previous studies such as [18] do not analyse to what extent changes in hidden  
77 model parameters, such as the time step and thresholds for cell rearrangement, can influence  
78 vertex configurations and other summary statistics. Here, we analyse a force-propagation im-  
79 plementation of vertex models [48, 49] as applied to a widely studied system in developmental  
80 biology, the larval wing disc of the fruit fly *Drosophila* [3, 4, 24]. We conduct convergence analy-  
81 ses of vertex positions with respect to all implementation-specific parameters of our model, and  
82 further analyse to what extent experimentally measurable summary statistics of tissue morphol-  
83 ogy, such as distributions of cell neighbour numbers and areas, depend on these parameters.

84 We find that vertex model predictions are sensitive to the length of cell cycle duration, the  
85 time step, and the size of the edge length threshold for cell rearrangement. Specifically, vertex  
86 configurations do not converge as the time step, the edge length threshold for cell rearrangement,

87 or the area threshold for cell removal are reduced. For example, reductions in the cell cycle  
88 duration may promote cell removal and reduce the size of the simulated tissue by up to a factor  
89 of two. We find that both the size of the time step and the size of the edge length threshold can  
90 influence the rate of cell rearrangement. Counterintuitively, the rate of cell removal is robust  
91 to changes in the area threshold for cell removal over multiple orders of magnitude. Further,  
92 analysing the active forces within the tissue reveals that vertices are subject to stronger forces  
93 during periods when cells grow and divide.

94 The remainder of the paper is organised as follows. In section 2, we describe our vertex  
95 model implementation of growth in the *Drosophila* larval wing disc. In section 3 we present our  
96 results. Finally, we discuss our results and draw conclusions for the use of cell-based models in  
97 quantitative biology in sections 4 and 5.

## 98 2 Methods

99 We consider a vertex model of the growing *Drosophila* wing imaginal disc, a monolayered  
100 epithelial tissue that is one of the most widely used applications of vertex models. The wing  
101 imaginal disc initially comprises around 30 cells, and undergoes a period of intense proliferation  
102 until there are around 10000 or more cells [3, 24]. Here, we outline the technical details of our  
103 model implementation. We start by introducing the equations of motion, then describe the  
104 initial and boundary conditions and implementations of cell growth and neighbour exchange.

105 **Equations of motion** In two-dimensional vertex models epithelial tissues are represented as  
106 tessellations of polygons that approximate the apical cell surfaces. We propagate the position  
107 of each vertex over time using an overdamped force equation, reflecting that cell junctions are  
108 not associated with a momentum. The force equation takes the form

$$\mu \frac{d\mathbf{x}_i}{dt} = -\nabla_i E, \quad (1)$$

109 where  $\mu$  is the friction strength,  $\mathbf{x}_i(t)$  is the position vector of vertex  $i$  at time  $t$ , and  $E$  denotes  
110 the total stored energy. The number of vertices in the system may change over time due to  
111 cell division and removal. The symbol  $\nabla_i$  denotes the gradient operator with respect to the

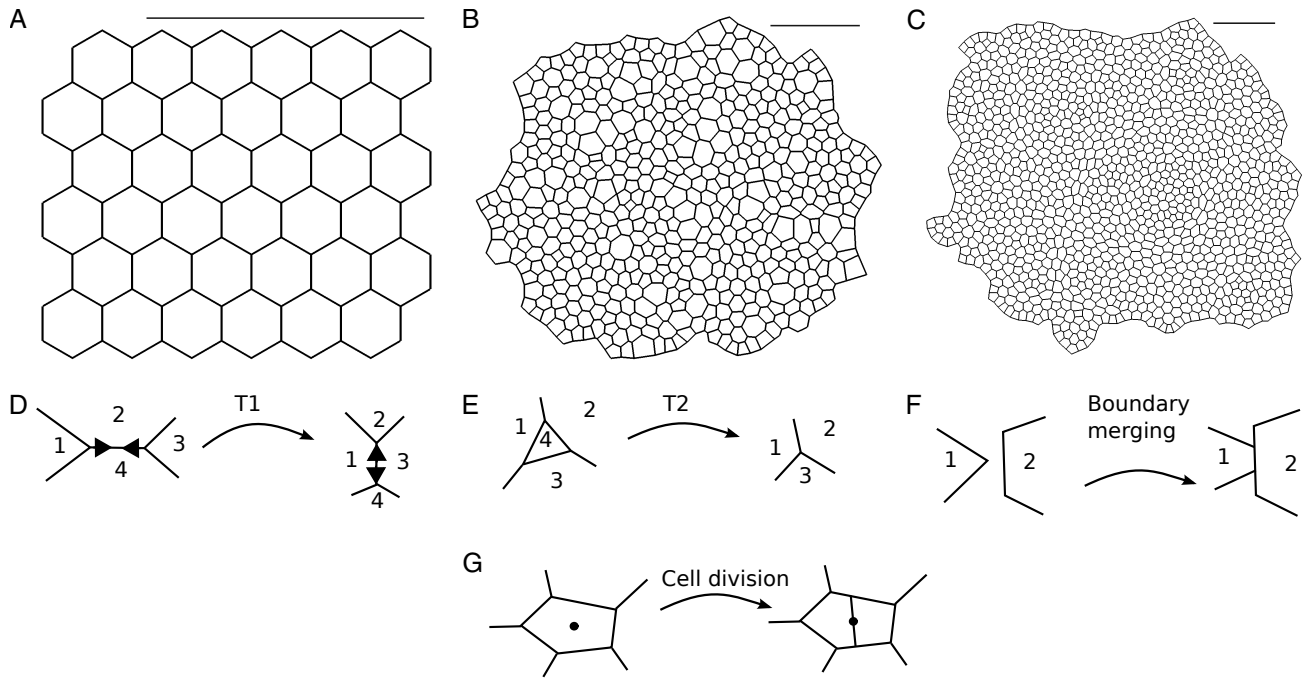


Figure 1: Two-dimensional vertex models represent cells in an epithelial tissue as polygons and allow different types of vertex rearrangement. (A-C) Snapshots of an example vertex model simulation used in our analysis. The growing *in silico* tissue undergoes four rounds of division. (A) The initial condition is a hexagonal packing of 36 cells. (B) Simulation progress after 6,750 time units at an intermediate stage of tissue growth. The tissue boundary is allowed to move freely and individual cells grow before division. (C) Snapshot of tissue at the end of the simulation at 27,000 time units. After the fourth (last) round of divisions the tissue relaxes into a stable configuration. Simulated tissues in (B-C) are rescaled to fit the view, a scale bar of fixed length is added for comparison. Simulation parameters are listed in table 1. Throughout the simulation, vertices may rearrange by T1 transitions (D), T2 transitions (E), boundary merging (F), and cell division (G).

112 coordinates of vertex  $i$ . The total stored energy takes the form

$$E = \sum_{\alpha} \frac{K}{2} (A_{\alpha} - A_{0,\alpha})^2 + \sum_{\langle i,j \rangle} \Lambda l_{i,j} + \sum_{\alpha} \frac{\Gamma}{2} P_{\alpha}^2. \quad (2)$$

113 Here, the first sum runs over every cell  $\alpha$  in the tissue,  $A_{\alpha}$  denotes the area of cell  $\alpha$  and  $A_{0,\alpha}$   
 114 is its target area. This term penalises deviations from the target area for individual cells, thus  
 115 describing cellular bulk elasticity. The second sum runs over all cell edges  $\langle i,j \rangle$  in the sheet and  
 116 penalizes long edges (we choose  $\Lambda > 0$ ), representing the combined effect of binding energy and  
 117 contractile molecules at the interface between two cells. The third sum also runs over all cells,  
 118 and  $P_{\alpha}$  denotes the perimeter of cell  $\alpha$ . This term represents a contractile acto-myosin cable  
 119 along the perimeter of each cell [3]. The parameters  $K$ ,  $\Lambda$ , and  $\Gamma$  together govern the strength

120 of the individual energy contributions.

121 Before solving the model numerically, we non-dimensionalise it to reduce the number of free  
 122 parameters [3]. Rescaling space by a characteristic length scale,  $L$ , chosen to be the typical  
 123 length of an individual cell, and time by the characteristic timescale,  $T = \mu/KL^2$ , equations  
 124 (1) and (2) become

$$\frac{d\mathbf{x}'_i}{dt'} = -\nabla'_i E', \quad (3)$$

$$E' = \sum_{\alpha} \frac{1}{2} (A'_{\alpha} - A'_{0,\alpha})^2 + \sum_{\langle i,j \rangle} \bar{\Lambda} l'_{i,j} + \sum_{\alpha} \frac{\bar{\Gamma}}{2} P'^2_{\alpha}, \quad (4)$$

125 where  $\mathbf{x}'_i$ ,  $A'_{\alpha}$ ,  $A'_{0,\alpha}$ ,  $l'_{i,j}$  and  $P'_{\alpha}$  denote the rescaled  $i^{\text{th}}$  vertex positions, the rescaled area and  
 126 target area of cell  $\alpha$ , the rescaled length of edge  $\langle i, j \rangle$ , and the rescaled cell perimeter of cell  
 127  $\alpha$ , respectively. The symbol  $\nabla'_i$  denotes the gradient with respect to the rescaled  $i^{\text{th}}$  vertex  
 128 position. In the non-dimensionalised model, cell shapes are governed by the rescaled target  
 129 area of each cell  $A'_{0,\alpha}$  and the rescaled mechanical parameters,  $\bar{\Lambda}$  and  $\bar{\Gamma}$ . For these parameters  
 130 we use previously proposed values [3], unless stated otherwise. A complete list of parameters  
 131 used in this study is provided in table 1.

132 To solve equations (3) and (4) numerically we use a forward Euler scheme:

$$\mathbf{x}'_i(t' + \Delta t') = \mathbf{x}'_i(t') - \nabla'_i E'(t') \Delta t'. \quad (5)$$

133 We analyse the dependence of simulation outcomes on the size of  $\Delta t'$  in the Results section.

134 **Initial and boundary conditions** Initially, the sheet is represented by a regular hexagonal  
 135 lattice of six by six cells (figure 1A). The boundary of the lattice is allowed to move freely  
 136 throughout the simulation. Each cell has initial area and target area  $A'^s = A'_0^s = 1$ , respectively.

137 **Cell neighbour exchange and removal** T1 transitions (figure 1D) are executed whenever  
 138 the length of a given edge decreases below the threshold  $l'_{T1} = 0.01$ . The length of the new edge,  
 139  $l_{\text{new}} = \rho l_{T1}$  ( $\rho = 1.5$ ), is chosen to be slightly longer than this threshold to avoid an immediate  
 140 reversion of the transition.

141 A second topological rearrangement in vertex models is a T2 transition, during which a

142 small triangular cell or void is removed from the tissue and replaced by a new vertex (figure  
143 1E). In our implementation any triangular cell is removed if its area drops below the threshold  
144  $A'_{T2} = 0.001$ . The energy function, equation (2), in conjunction with T2 transitions can be  
145 understood as a model for cell removal: cells are extruded from the sheet by a T2 transition if  
146 the energy function, equation (2), leads to a sufficiently small cell. Note that in equation (2) the  
147 bulk elasticity or area contribution of a cell  $\alpha$  is finite even when the area  $A_\alpha$  is zero, allowing  
148 individual cells to become arbitrarily small if this is energetically favourable. As cells decrease  
149 in area they typically also reduce their number of sides. Hence it is sufficient to remove only  
150 small triangular cells instead of cells with four or more sides [3, 4, 24].

151 We further model the merging of overlapping tissue boundaries (figure 1F). Whenever two  
152 boundary cells overlap, a new edge of length  $l_{\text{new}}$  is created that is shared by the overlapping  
153 cells. In cases where the cells overlap by multiple vertices, or if the same cells overlap again  
154 after a previous merging of edges, the implementation ensures that two adjacent polygons never  
155 share more than one edge by removing obsolete vertices. The merging of boundary edges is  
156 discussed in further detail in [48].

157 **Cell growth and division** Unless stated otherwise the tissue is simulated for  $n_d = 4$  rounds  
158 of division, i.e. each cell divides exactly  $n_d$  times. To facilitate comparison with previous simu-  
159 lations of the wing disc where vertices were propagated by minimising the energy function (2),  
160 we model each cell to have two cell cycle phases: quiescent and growing. The duration of the  
161 first, quiescent, phase of the cell cycle is drawn independently from an exponential distribution  
162 with mean  $2t'_l/3$ , where  $t'_l$  is the total cell cycle duration. We choose stochasticity in this phase  
163 of the cell cycle to avoid biologically unrealistic synchronous adjacent divisions; this also helps  
164 keeping the simulations in a quasistatic regime. The duration of the second, growing, phase  
165 of the cell cycle is fixed at length  $t'_l/3$  for each cell. During this time the target area,  $A'_{0,\alpha}$ , of  
166 the cell grows linearly to twice its original value. Upon completion of the growth phase, the  
167 cell divides. We choose a fixed duration for the growth phase to ensure gradual, quasistatic cell  
168 growth. Two-stage cell cycles with an exponentially distributed and a fixed length contribution  
169 have previously been observed in various cell cultures [50, 51] and have been applied to model  
170 growth in the *Drosophila* wing imaginal disc [27].

171 At each cell division event, a new edge is created that separates the newly created daughter

172 cells. The new edge is drawn along the short axis of the polygon that represents the mother  
173 cell [48]. The short axis has been shown to approximate the division direction (cleavage plane)  
174 of cells in a variety of tissues [52], including the *Drosophila* wing imaginal disc [53]. The short  
175 axis of a polygon crosses the centre of mass of the polygon, and it is defined as the axis around  
176 which the moment of inertia of the polygon is maximised. Each daughter cell receives half the  
177 target area of the mother cell upon division.

178 Applying this cell cycle model, we let the tissue grow for  $n_d = 4$  generations. Each cell of  
179 the last generation remains in the quiescent phase of the cell cycle until the simulation stops.  
180 We select the total simulation time  $t'_{\text{tot}} = 27,000$ , unless specified otherwise. This duration  
181 is chosen such that the tissue can relax into its equilibrium configuration after the final cell  
182 division.

183 **Computational implementation** We implement the model within Chaste, an open source  
184 C++ library that provides a systematic framework for the simulation of vertex models [48,  
185 49]. Our code is available in the supplementary material as a zip archive. Pseudocode for  
186 our implementation is provided in algorithm 1. Each time step starts by updating the cell  
187 target areas. Then, cell division, removal (T2 transitions), rearrangement (T1 transitions), and  
188 boundary merging are performed before incrementing the simulation time. The algorithm stops  
when the end time of the simulation is reached.

```
Initialize time  $t' = 0$ ;  
Generate initial configuration;  
while  $t' < t'_{\text{tot}}$  do  
    1. Update cell target areas;  
    2. Perform cell division on cells that have reached the end of their cell cycle;  
    3. Perform any T2 transitions;  
    4. Perform any T1 transitions;  
    5. Perform boundary merging;  
    6. Propagate vertex positions using equation (3);  
    7. Increment time by  $\Delta t'$ ;  
end
```

**Algorithm 1:** Pseudocode of the simulation algorithm.

189

Table 1: **Description of parameter values used in our simulations.**

Parameter	Description	Value	Reference
$\bar{\Lambda}$	Cell-cell adhesion coefficient	0.12	[3]
$\bar{\Gamma}$	Cortical contractility coefficient	0.04	[3]
$\Delta t'$	Time step	0.01	[48]
$A'_{\min}$	T2 transition area threshold	0.001	[48]
$l'_{T1}$	T1 transition length threshold	0.01	[48]
$\rho$	New edges after a T1 transition have the length $l'_{\text{new}} = \rho l'_{T1}$	1.5	[48]
$A'^s$	Initial cell area	1.0	[3]
$A'_0^s$	Initial cell target area	1.0	[3]
$N^s$	Initial cell number	36	[3]
$t'_l$	Mean cell cycle duration	1,750	–
$t'_{\text{tot}}$	Simulation duration	27,000	–
$n_d$	Total number of divisions per cell	4	–

For parameter values for which no reference is given, please see main text for details on how these values were estimated. Spatial and temporal parameters are non-dimensionalised (see section 2 for details).

### 190 **3 Results**

191 In this section, we analyse how the model behaviour depends on implementation parameters.  
 192 Vertex models are typically used to predict summary statistics of cellular packing and growth,  
 193 such as the distribution of cell neighbour numbers and areas [3, 24]. We analyse how these  
 194 summary statistics may depend on simulation parameters. Specifically, we focus on the final  
 195 cell number of the simulation, the total tissue area, the numbers of cell rearrangements (T1  
 196 transitions) and cell removals (T2 transitions), the distribution of cell neighbour numbers, and  
 197 the correlation between cell neighbour number and cell area. Note that we exclude cells on the  
 198 tissue boundary from statistics of cell neighbour numbers in order to avoid boundary artefacts.

#### 199 **Tissue size is sensitive to cell cycle duration**

200 In previous vertex model applications [3, 4, 24], experimentally measured summary statistics of  
 201 cellular packing were reproduced using an energy-minimisation implementation. Such energy  
 202 minimisation schemes assume quasistatic evolution of the sheet. It is unclear to what extent  
 203 summary statistics are preserved when the tissue evolves in a dynamic regime.

204 We analyse the dependence of the summary statistics on the cell cycle duration,  $t'_l$ , in  
 205 figure 2. The cell number and tissue area at the end of the simulation, and the total number

206 of cell rearrangements, vary by up to a factor of two as the mean cell cycle duration increases  
207 from five to 2000. The cell number and tissue area increase with the mean cell cycle duration,  
208 whereas the amount of rearrangement decreases, reflecting a reduction in cell removal events.  
209 The cell number, tissue area, and the total number of cell rearrangement converge for mean cell  
210 cycle durations of 1500 or longer.

211 The cell neighbour number distribution depends on the cell cycle duration in a non-linear  
212 fashion. For example, the number of hexagons peaks at cell cycle durations of 10 as well as  
213 at 1000 time units. For cell cycle durations longer than 1000 rescaled time units the numbers  
214 of pentagons and heptagons increase as the cell cycle duration increases, while the number  
215 of hexagons decreases. We interpret this non-linear dependence as resulting from changes in  
216 cell neighbour numbers due to cell division and due to cell neighbour exchanges. As the cell  
217 cycle duration exceeds  $t'_l = 10$ , a decrease in the number of cell removal events leads to an  
218 increase in cell division events which, in turn, drives the polygon distribution away from its  
219 hexagonal initial condition. As the number of cell divisions ceases to increase the number of cell  
220 rearrangements drops as well, and the number of hexagons reach a second peak. Increasing the  
221 time between cell divisions further decreases the number of hexagons. Note that none of the  
222 simulated polygon histograms coincide with previously reported histograms in which pentagons  
223 outweigh hexagons [3, 24], despite choosing identical parameters in energy equation (2). We  
224 discuss possible reasons for this difference in section 4.

225 A further summary statistic of cellular packing is the mean area for cells of each polygon  
226 number. This summary statistic often used to characterise epithelia [3, 25, 54, 55]. We find that  
227 the mean cell area for each polygon number is not sensitive to changes in cell cycle length and  
228 increases monotonically with polygon number.

229 Differences in tissue size and cellular packing arise due to a sensitive interplay between the  
230 cell cycle duration and the timescale for mechanical relaxation of the tissue,  $T$ . Growing cells  
231 push against their neighbours, leading to tissue growth. This outward movement is counter-  
232 acted by the friction term in the force equation (1). As cells grow more quickly, i.e. with  
233 smaller cell cycle durations, the force required to push the surrounding cells outward increases.  
234 For sufficiently small cell cycle durations, the forces may become strong enough to cause cell  
235 extrusion.

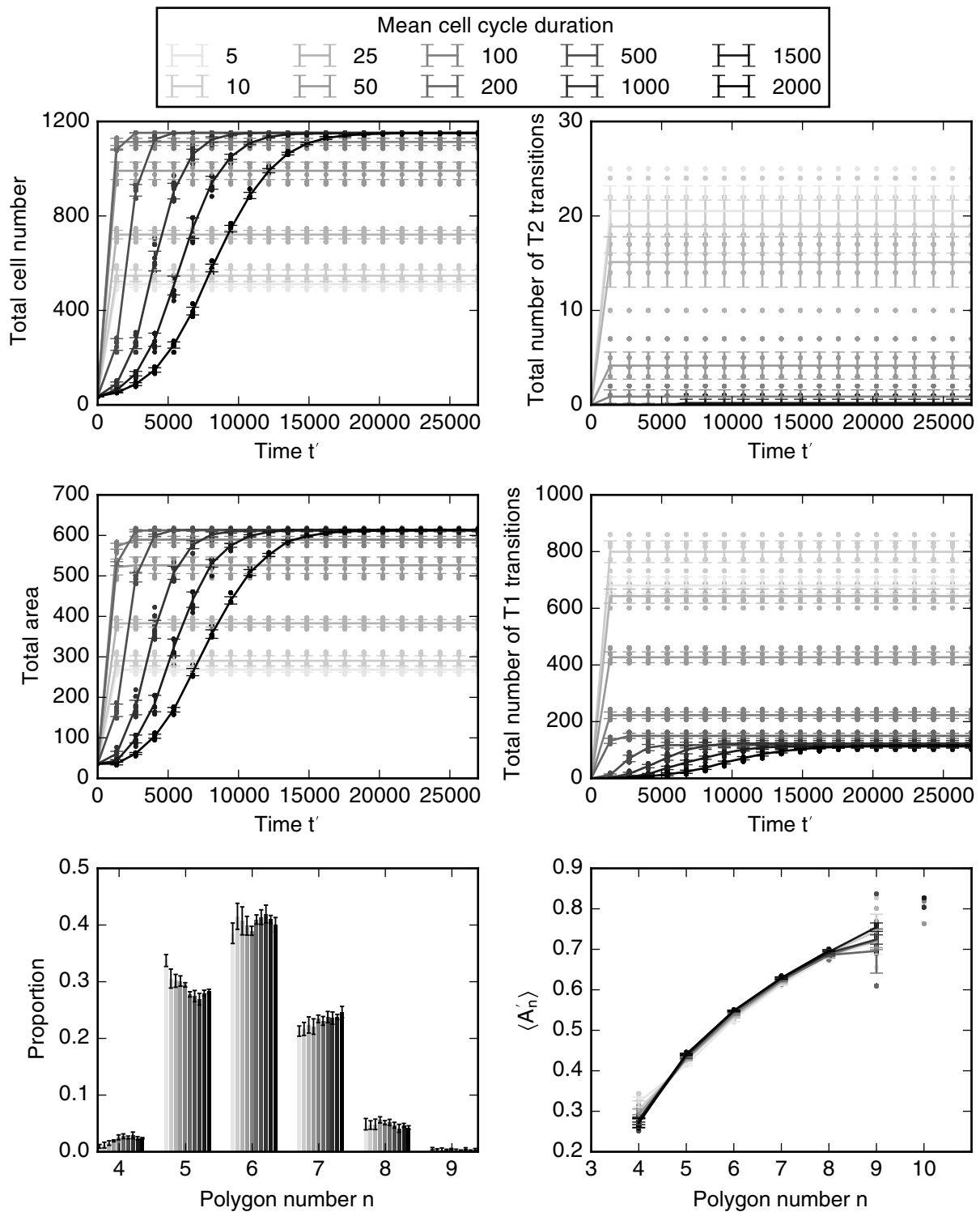


Figure 2: Variation of cell numbers, number of T2 transitions, tissue area, total number of T1 transitions, cell neighbour number distribution and mean area per polygon class with mean cell cycle duration. Error bars denote standard deviations across 100 simulations. All simulation parameters are provided in table 1.

## 236 Cell growth and division increase forces within the tissue

237 The energy expression (2) leads to three different force contributions on each node: an area  
238 force; an edge force; and a perimeter force. In figure 3 we analyse the magnitude of these  
239 contributions for a simulation with mean cell cycle duration  $t'_i = 2000$ . The solid line represents  
240 the average magnitudes for the individual contributions for all forces in the tissue, and the  
241 shaded areas mark one standard deviation. The strongest force contribution is the area force,  
242 whereas the weakest is the edge force. This relationship is intuitive. Most cells in the tissue have  
243 areas smaller than their target area of 1.0 (compare with figure 2). Hence, for an individual cell  
244 the area force contribution points outwards from the cell. The edge contribution and perimeter  
245 contribution point inwards for individual cells, thus counteracting the area force. The variation  
246 of each force contribution has the same order of magnitude as their mean values, illustrating  
247 that the forces on nodes can vary strongly across the tissue. The force magnitudes change  
248 throughout the simulation, and they peak at a value that is 50% higher than the final values.  
249 For times larger than 15000 time units, the forces do not change with time in figure 3. At  
250 this time cells stop dividing and the final cell number is reached, illustrating that the forces  
251 are largest when the tissue size is increasing most rapidly. This transient rise in forces emerges  
252 as cells in the interior of the simulated tissue push on their neighbours as they grow before  
253 division. This predicts that cells undergoing active processes, such as growth and division, are  
254 subject to significantly higher forces than cells in quiescent tissues.

## 255 Large time steps suppress cell rearrangement

256 When using an explicit Euler method, such as as in equation (5), the time step must be cho-  
257 sen sufficiently small to provide a stable and accurate numerical approximation of the model  
258 dynamics. To this end, we conduct a convergence analysis. To reduce simulation times, we  
259 conduct the convergence analysis on sample simulations in which each cell divides  $n_d = 3$  times  
260 instead of four, and with total simulation time  $t'_{\text{tot}} = 21000$ . We choose a series of decreasing  
261 time steps  $\Delta t'_i$  and define the error function

$$\epsilon_i^t = \left\| \sum_j \mathbf{x}_j^i - \sum_j \mathbf{x}_j^{i-1} \right\|, \quad (6)$$

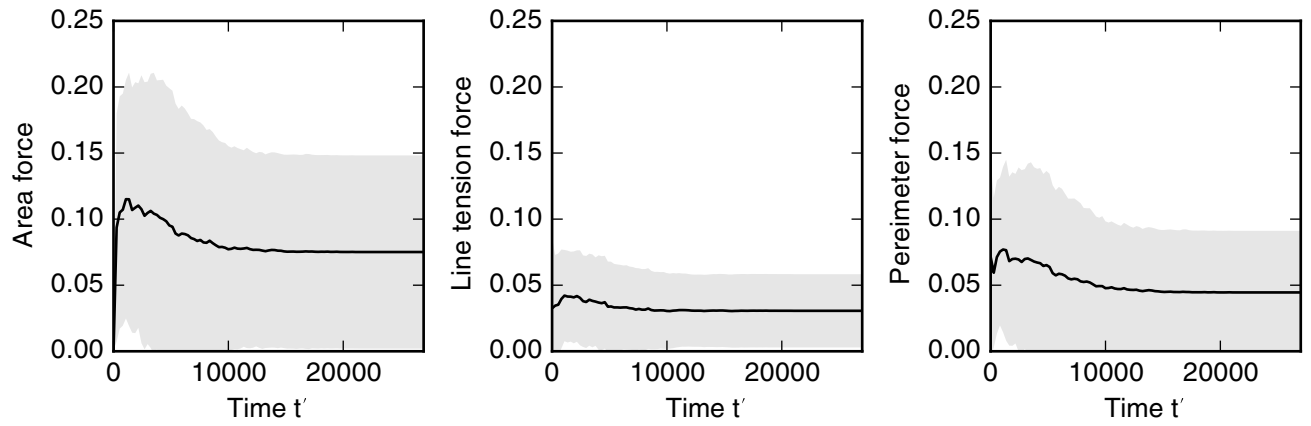


Figure 3: Magnitude of area, edge, and perimeter force contributions over time. The solid lines represent the average of force contribution magnitudes across all nodes for one simulation. The shaded regions represent one standard deviation of the force contribution magnitudes across the tissue. A cell cycle duration of  $t'_l = 2000$  is used. All other parameters are listed in table 1.

262 where the sums run over all vertex positions,  $\mathbf{x}_j^i$ , at the end of the simulation with time steps  
263  $\Delta t'_i$  and  $\Delta t'_{i-1}$ . The error function (6) evaluates the differences between the sums of final  
264 vertex positions at decreasing values of the time step. In order to ensure that simulations  
265 with consecutive values of the time step follow identical dynamics we generate fixed series of  
266 exponentially distributed random variates from which we calculate the cell cycle durations. We  
267 analyse the convergence of the vertex positions in the time step  $\Delta t'$  in figure 4. In general,  
268 the error function does not converge. However, for most simulations the error function (6)  
269 assumes values smaller than  $10^{-1}$  for time steps smaller than  $10^{-2}$ . Note that this time step  
270 is five orders of magnitudes smaller than the average cell cycle duration. When the time step  
271 is larger than  $10^{-2}$  the error function (6) is large since a significant number of T1 transitions  
272 are suppressed. On rare occasions, the error function may be non-negligible even if the time  
273 step is smaller than  $10^{-2}$ . These large values of the error function (6) reflect changes in the  
274 number of T1 transitions as the time step decreases. When the time step is smaller than  $10^{-2}$   
275 summary statistics of cellular packing, such as the distribution of cell neighbour numbers or the  
276 total number of cells, do not change as the time step is decreased further.

277 An example of how differences in the number of T1 transitions and final vertex positions can  
278 emerge when the time step is smaller than  $10^{-2}$  is shown in figure 5. In this figure, a cell division  
279 occurs in simulations using a time step of 0.004 and 0.002. Both simulation use the same, fixed,  
280 series of cell cycle times and vertex positions in both simulations are similar over time up to  
281 the time point of the illustrated division. Here, and throughout, cells divide along their short  
282 axis. In this example, the short axis of the cell intersects the cell boundary close to an existing  
283 vertex. Due to differences in the vertex positions of the cell, the new vertex is created on different  
284 cell-cell interfaces as the the size of the time step varies. As the simulation progresses, these  
285 different vertex configurations propagate towards different final tissue configurations, leading to  
286 differences in the total number of T1 transitions and the error function. In figure 4, differences  
287 in final vertex positions are observed for all considered values of the time step. However, such  
288 differences in vertex positions do not propagate through to tissue level summary statistics such  
289 as the distribution of cell neighbour numbers or areas.

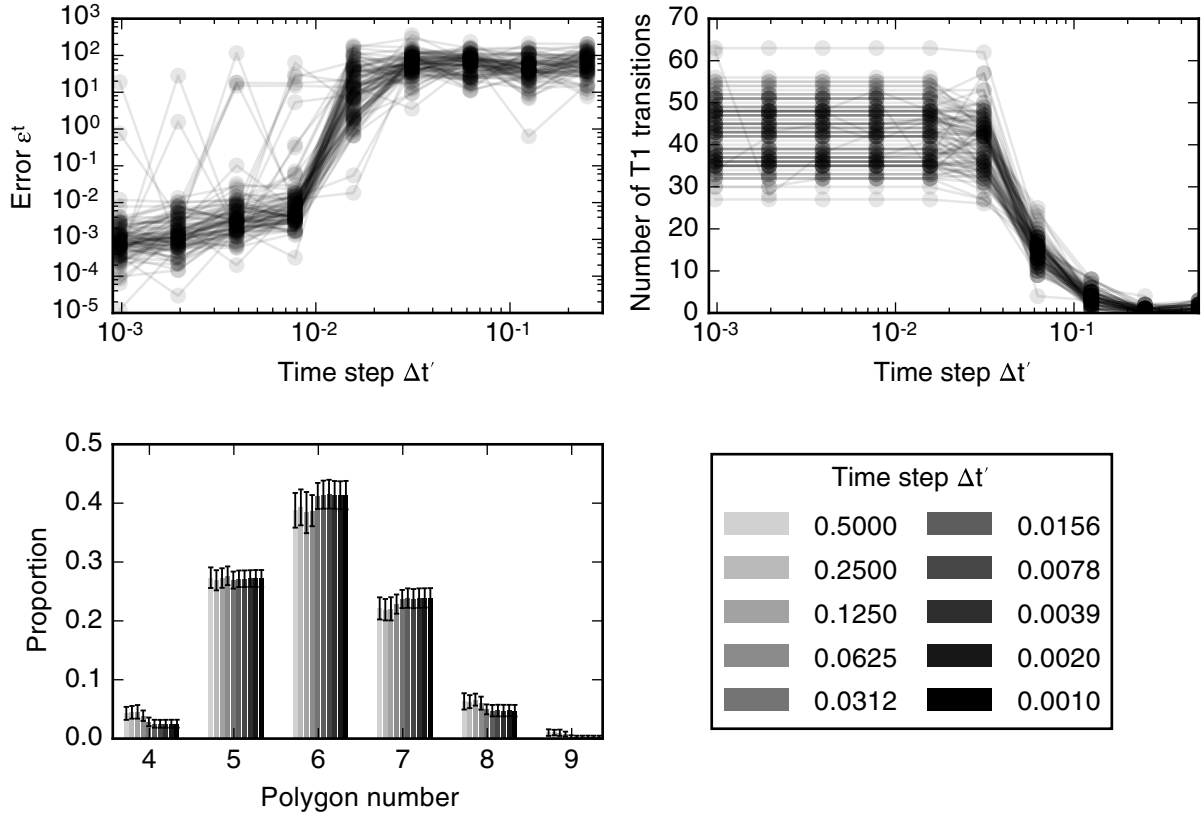


Figure 4: Variation in simulation result with the time step. The error function decreases as the time step is decreased. The number of T1 transitions in the simulations is stable for time steps smaller than 0.02 and decreases with time steps longer than 0.002. For time steps  $\Delta t' < 0.02$  the cell neighbour number distribution is stable; the means of individual polygon class proportions vary by less than 0.01. In these simulations, cells undergo  $n_d = 3$  rounds of division, and the total simulation time is  $t'_{\text{tot}} = 21000$ . All other parameter values are listed in table 1. Error bars denote standard deviations across 100 simulations.

## 290 Occurrence of cell rearrangements is regulated by rearrangement threshold

291 We further analyse the dependence of vertex positions and summary statistics on the T1 transi-  
 292 tion threshold,  $l'_{T1}$ . Similar to the time step convergence analysis we define a series of decreasing  
 293 values of  $l'_{T1,i}$  and the error function

$$\epsilon_i^{T1} = \left\| \sum_j \mathbf{x}_j^i - \sum_j \mathbf{x}_j^{i-1} \right\|, \quad (7)$$

294 which measures the difference between the final vertex positions of simulations with decreasing  
 295 values of the T1 transition threshold,  $l'_{T1,i}$ . The variation of the error function with decreasing  
 296 values of  $l'_{T1,i}$  is shown in figure 8. For all considered values of  $l'_{T1}$  the error function does not

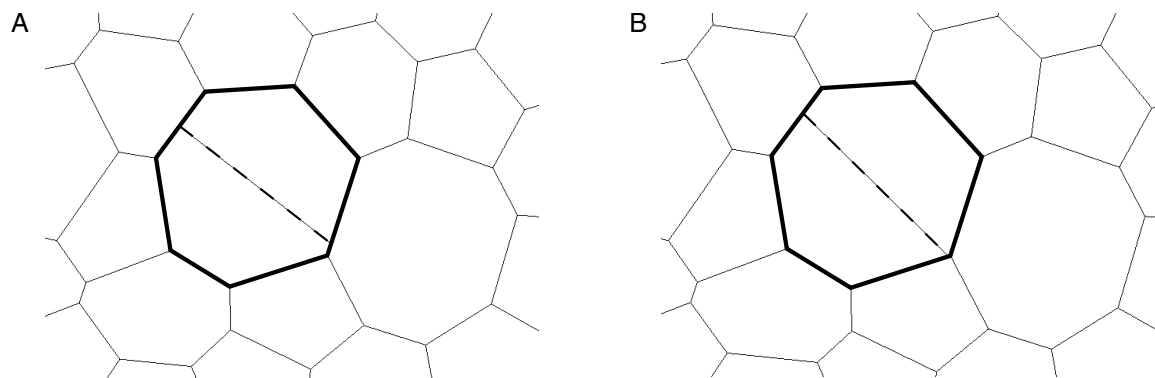


Figure 5: Differences in vertex configurations can arise from simulations run with different temporal resolution. A dividing cell in simulations run with time steps  $\Delta t = 0.004$  (A) and  $\Delta t = 0.002$  (B) is shown in bold. During the cell division, a new cell-cell interface (dashed line) is created along the short axis of the dividing cell by creating new vertices (see Methods section for details). The daughter cells of the dividing cell contain different vertices in the configurations corresponding to the two time steps. This leads to different vertex configurations at the end of the simulations.

297 converge and varies between values of 1 and  $10^3$ . Only for  $l'_{T1} < 10^{-3}$  is the error function (7)  
298 smaller than one for some simulations. However, for such small values of  $l'_{T1}$ , many simula-  
299 tions fail as the simulation algorithm encounters situations that it cannot resolve, for example  
300 configurations including overlapping cells.

301 A large T1 transition threshold of 0.2 length units leads to a large number of T1 transitions,  
302 whereas T1 transitions are suppressed for thresholds of 0.003 length units or smaller. This vari-  
303 ation in the amount of cell rearrangement influences summary statistics of cellular packing, for  
304 example leading to variations in the cell neighbour number distribution. For large rearrange-  
305 ment thresholds, e.g.  $l'_{T1} = 0.2$ , the number of cell rearrangements is high, leading to a high  
306 proportion of hexagons (around 0.6), whereas suppression of cell rearrangements for small cell  
307 rearrangement thresholds, for example  $l'_{T1} = 0.2$ , leads to a wider distribution of cell neighbour  
308 numbers with a proportion of hexagons (below 0.4). The number of cell rearrangements is stable  
309 between T1 transition thresholds of 0.02 and 0.003. In this regime, the proportion of hexagons  
310 varies slightly between 0.425 and 0.409. Despite the stable number of T1 transitions across this  
311 parameter regime between 0.02 and 0.003 the final vertex positions differ for any two values of  
312 the T1 transition threshold, as reflected in values of the error function.

313 If the T1 transition threshold is smaller than 0.001 simulations fail to complete. An example  
314 of how a simulation can fail due to a small value of the T1 transition threshold is provided in  
315 figure 7. A snapshot is taken of the simulation at the last two time steps before simulation

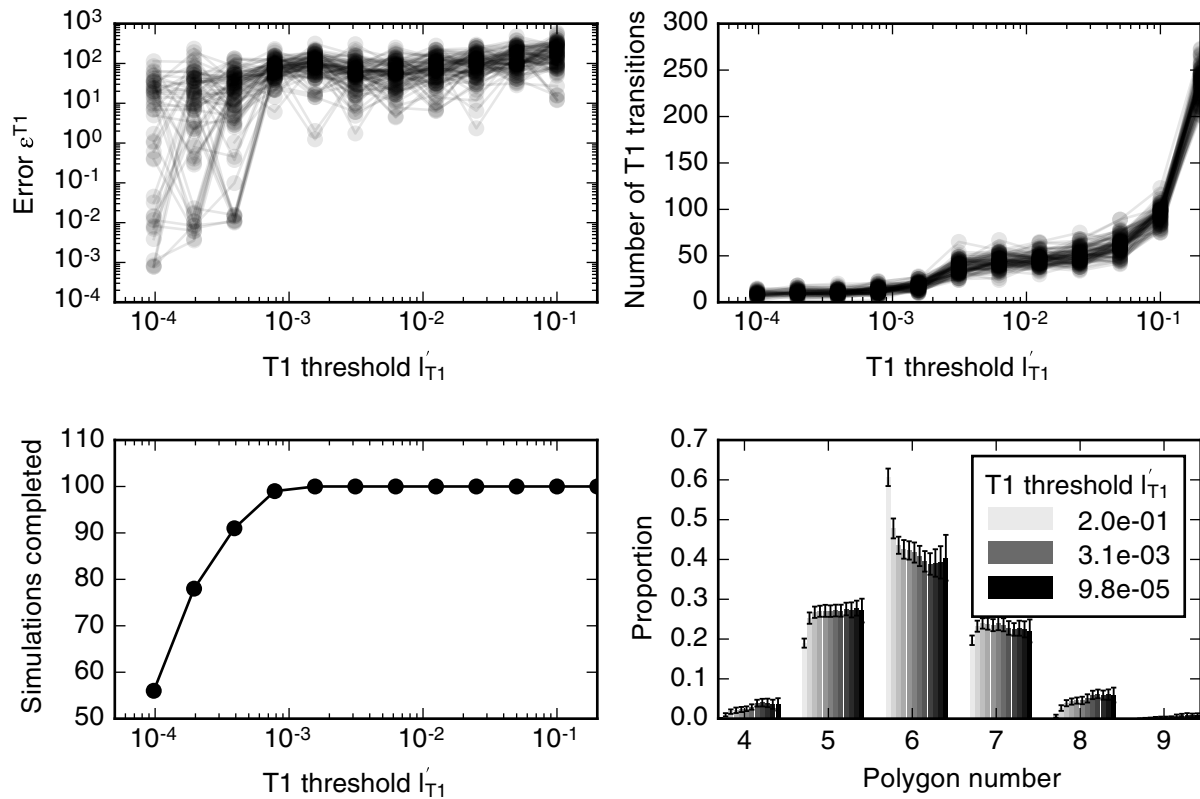


Figure 6: Variation of simulation result with size of the T1 transition threshold,  $l'_{T1}$ . The error function (7) does not converge as  $l'_{T1}$  decreases. The number of cell rearrangements is larger than 100 for a large value of the rearrangement threshold  $l'_{T1} > 0.1$ , whereas cell rearrangement is suppressed for small values of the rearrangement threshold  $l'_{T1} < 0.001$ , with cell rearrangement numbers less than 30. When cell rearrangement is suppressed, simulations fail to complete. Varying amounts of cell rearrangement lead to different distributions of cell neighbour numbers. All simulation parameters are listed in table 1. Error bars denote standard deviations across 100 simulations.

316 failure. Due to a short edge two boundary vertices in the tissue appear merged (arrow in figure  
 317 7A). This short edge is magnified for the penultimate (figure 7B) and last time step (figure 7C)  
 318 before simulation failure. At the last time step, one of the boundary cells becomes concave. The  
 319 simulation then fails since our vertex model implementation cannot resolve this configuration.  
 320 When two boundary cells overlap, the simulation procedure attempts to merge the vertex with  
 321 its closest cell boundary. This procedure fails because the identified boundary is internal to the  
 322 tissue rather than a boundary interface.

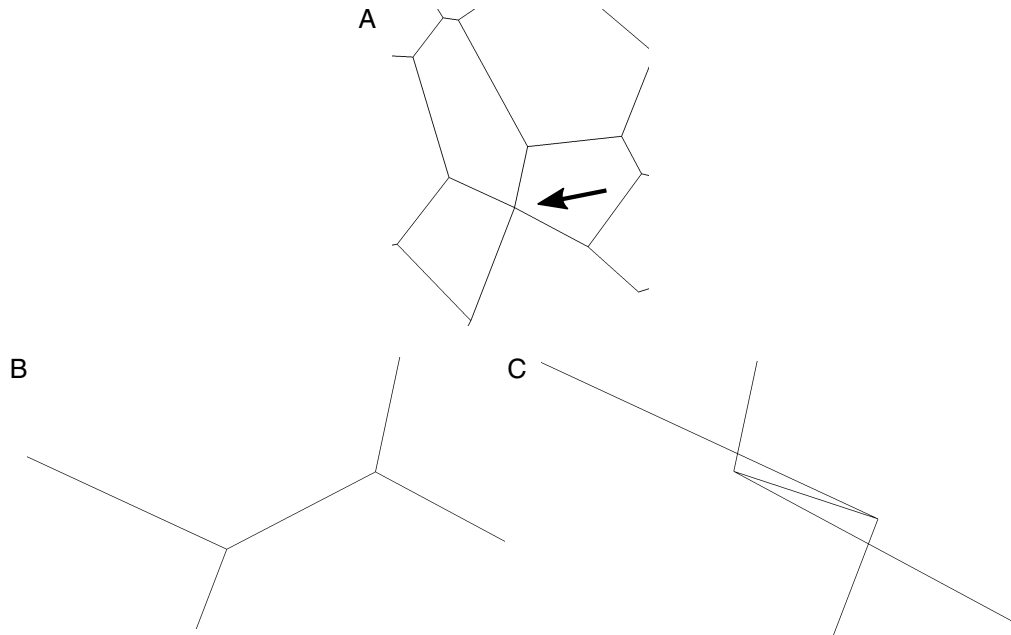


Figure 7: Small values of the T1 transition threshold,  $l'_{T1} < 10^{-3}$ , suppress rearrangement and lead to failure of the simulation algorithm. One of the failing simulations in figure 8 is analysed. The tissue configuration in the last time step before simulation failure contains two vertices that appear to be merged due to a short edge on the tissue boundary. The short edge is indicated by an arrow (A) and magnified for the penultimate (B) and final time step (C) of the simulation. Since the short edge in the penultimate time step is prevented from rearranging, the two adjacent boundary cells intersect each other, leading to failure of the simulation.

### 323 **Simulation results are robust to variation in length of newly formed edges.**

324 When cells exchange neighbours by way of T1 transitions, new edges are formed. New edges  
 325 have length  $l'_{\text{new}} = \rho l'_{T1}$ . In order to investigate the extent to which changes in the length of  
 326 newly formed edges can affect simulation results we define a series of increasing values for  $\rho^j$   
 327 and the error function

$$\epsilon_i^\rho = \left\| \sum_j \mathbf{x}_j^i - \sum_j \mathbf{x}_j^0 \right\|, \quad (8)$$

328 which measures the difference in vertex positions relative to simulations with  $\rho^0 = 1.05$ . We find  
 329 that individual simulations may result in different final tissue configurations than the reference  
 330 configuration if newly formed edges are twice as long as the rearrangement threshold or longer.  
 331 Such differences in configuration were observed for three out of 100 simulations, illustrating the  
 332 robustness of simulation results to the length of newly formed edges.

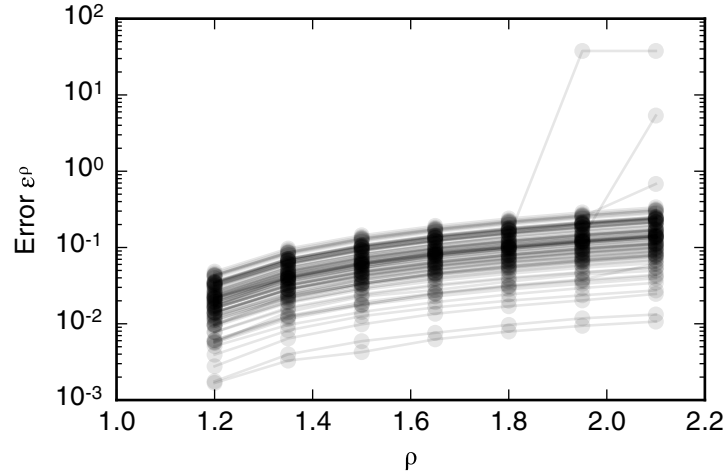


Figure 8: Dependence of simulation results on the length of edges created by T1 transitions,  $l'_{\text{new}} = \rho l'_{\text{T1}}$ . The error function (8) is recorded for 100 simulations. All simulation parameters are listed in table 1. The error function is smaller than 1 for for  $\rho < 2.0$ .

333 **Rate of T2 transitions is robust to variation in the T2 transition threshold**  
 334 **over five orders of magnitude**

335 Next, we turn to the value of the T2 transition threshold. We define a series of decreasing values  
 336 of  $A'_{\text{T2}}^i$  and the error function

$$\epsilon_i^{\text{T2}} = \left\| \sum_j \mathbf{x}_j^i - \sum_j \mathbf{x}_j^{i-1} \right\|, \quad (9)$$

337 which measures the difference between the final vertex positions of simulations with decreasing  
 338 values of the T2 transition threshold,  $A'_{\text{T2}}^i$ . In order to analyse the value of the error function  
 339 (9) in a simulation with a significant amount of cell rearrangement we run simulations with  
 340  $n_d = 7$  generations, a cell cycle duration of  $t'_l = 700$ , and total simulation time  $t'_{\text{tot}} = 19600$ .  
 341 All further simulation parameters are listed in table 1.

342 The value of the error function, on average, is small in figure 9. However, the error function  
 343 does not converge for individual simulations and may be large between consecutive values of  
 344 the threshold. In particular, the error function does not converge to zero. As the threshold  
 345 decreases, the overall number of T2 transitions in the simulations is stable at approximately  
 346 150 T2 transitions per simulation. However, for individual simulations the total number of T2  
 347 transitions may vary by up to 10 as the threshold  $A'_{\text{T2}}$  is decreased. The overall number of T2

348 transitions does not change over a large range of T2 transition thresholds that covers multiple  
 349 orders of magnitude, and all simulations complete without errors even if the T2 transition  
 350 threshold is smaller than  $10^{-6}$ , which is three orders of magnitudes smaller than the standard  
 351 value for this parameter in our simulations. The independence of the number of T2 transitions of  
 352 the threshold  $A_{T2}^i$  is reflected in tissue-level summary statistics, such as the distributions of cell  
 neighbour numbers numbers, which are unaffected by changes in the T2 transition threshold.

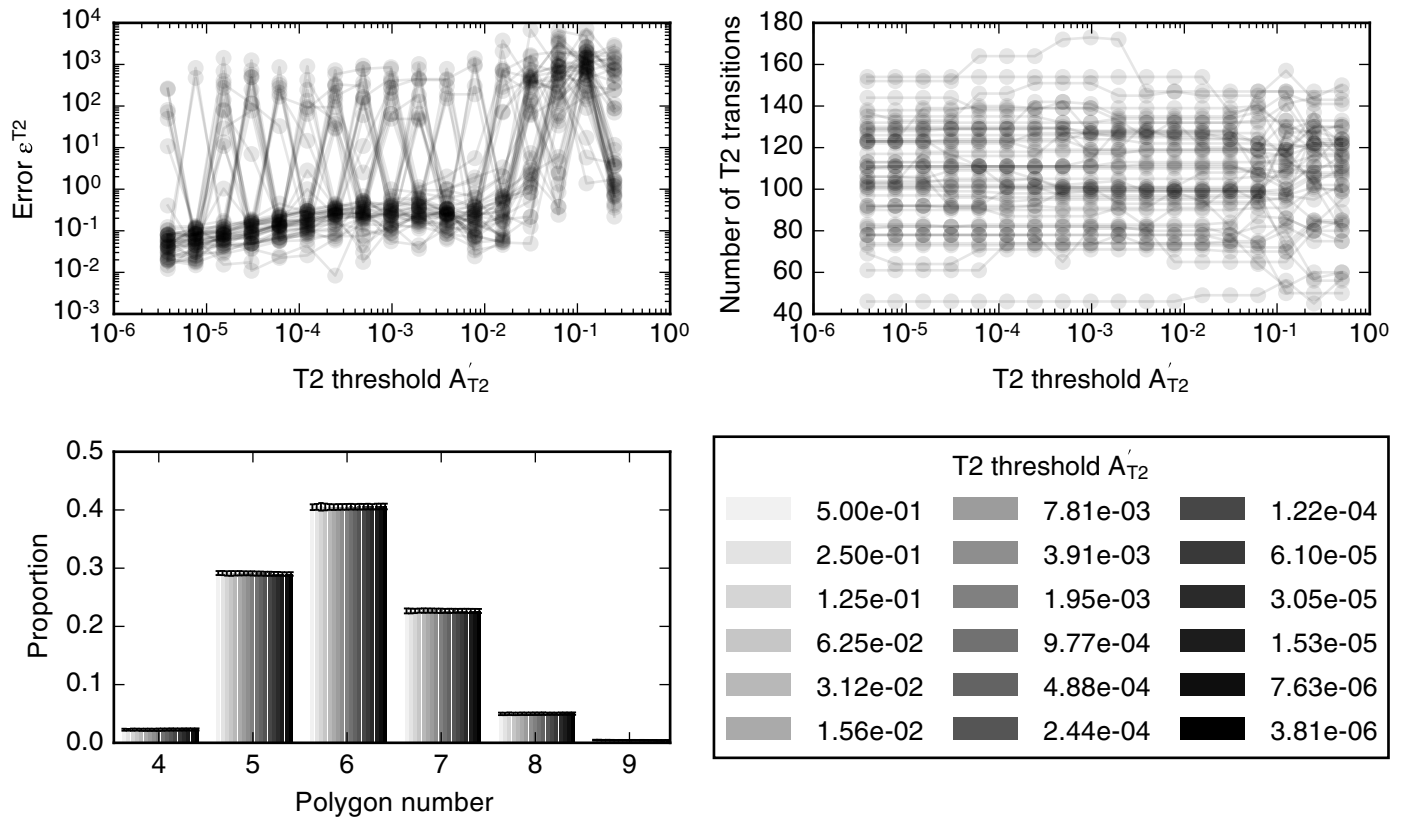


Figure 9: Dependence of simulation results on the T2 transition threshold,  $A_{T2}^i$ . The error function (9) assumes values less than one for  $A_{T2} < 10^{-2}$ . The total number of T2 transitions per simulation is stable for all observed values of  $A_{T2}$ . Tissue-level summary statistics such as the cell neighbour number distribution are not affected by changes in the threshold. Error bars denote standard deviations across 50 simulations. Simulations are run with  $n_d = 7$  rounds of division, a cell cycle duration of  $t_l^i = 700$ , and total simulation time  $t_{tot}^i = 19600$ . All further simulation parameters are listed in table 1.

353

354 Finally, we investigate whether the update ordering within algorithm 1 may affect simulation  
 355 results. To this end, we randomise the order in which T1 transitions are conducted during one  
 356 time step. We find that the update order does not lead to differences in final vertex positions  
 357 in 100 simulations. This is intuitive, considering that the order in which individual events are

358 conducted is most likely to be relevant in situations where events happen directly adjacent to  
359 each other, for example if two adjacent edges undergo T1 transitions at the same time step, if  
360 there are two adjacent divisions, or if a dividing cell also participates in cell rearrangement. In  
361 these examples, the order in which these events occur during one time step may have an impact  
362 on simulation outcomes. Our results imply that no adjacent two edges undergo T1 transitions  
363 in 100 sample simulations.

## 364 4 Discussion

365 Cell-based models have the potential to help unravel fundamental biophysical mechanisms un-  
366 derlying the growth and dynamics of biological tissues. However, the numerical implementation  
367 of such models is rarely analysed and the dependence of model predictions on implementation  
368 details often remains unknown. Here, we analyse a widely applied class of cell-based mod-  
369 els called a vertex model, and probe to what extent experimentally relevant summary statistics  
370 can depend on implementation details, such as choice of timescales or numerical implementation  
371 parameters.

372 For example, we find that the speed with which cells grow and divide relative to the timescale  
373 of tissue relaxation can significantly alter the *in silico* tissue behaviour. The total number cells  
374 in the tissue, as well as the tissue area and the amount of cell rearrangement, vary by up to a  
375 factor of two as the mean cell cycle duration is changed. Summary statistics of cellular packing,  
376 such as the distribution of cell neighbour numbers, or the correlation between cell neighbour  
377 number and area, are less strongly affected by the exact choice of timescale; the main features  
378 of these statistics are preserved in all cases.

379 The distribution of cell numbers for the case of quasistatic simulations differs from previously  
380 reported results [3]. Specifically, we observe fewer pentagons than hexagons. This discrepancy  
381 might arise from a difference in how equation (2) is used to evolve the tissue. For example,  
382 our implementation of the cell cycle differs from other implementations where the cell cycle  
383 duration varies spatially in the tissue [4, 27, 38]. Further, in [3], a global energy minimisation  
384 scheme is used to propagate vertex positions, whereas a force-based approach is used here. A  
385 major difference between the two approaches is the fraction of cells in the tissue that are allowed  
386 to divide concurrently. In our implementation, up to one third of the cells undergo cell-growth

387 at any given time, whereas in previous implementations all cells grow and divide sequentially.  
388 Further analysis is required to understand to what extent synchronous growth and division  
389 can affect cellular packing in epithelial tissues. Milan et al. report that up to 1.7% of cells in  
390 the early wing disc are mitotic at any given time [56]. However, mitosis and cell growth may  
391 not happen consecutively, hence the optimal choice of the duration of the growth phase in our  
392 simulations is unclear. Overall, it is unclear to what extent different choices for the cell cycle  
393 model may influence summary statistics of cellular packing.

394 Our analysis of forces throughout our simulations in figure 3 reveals that, on average, the  
395 area force contribution is stronger than the edge force contribution and the perimeter force  
396 contribution on a given node. Further, forces on cells increase during phases of proliferation  
397 and growth. Our findings may be of relevance to force-inference approaches that estimate  
398 forces using segmented microscopy images of epithelial tissues [57–59]. Force-inference methods  
399 often assume that the measured configuration of cells is assumed to be in equilibrium. It is  
400 unclear to what extent force-inference approaches introduce errors if this is not the case. In our  
401 simulations, forces are up to 50% higher when simulations are run in a dynamic regime, where  
402 cells grow and divide, than in the static regime at the end of the simulation, where cells are  
403 relaxed into a static configuration.

404 The vertex positions, as well as simulation summary statistics, vary as the time step of  
405 the simulation is changed, and differences in vertex positions decrease with the time step.  
406 Counterintuitively, large time steps can suppress cell rearrangement in vertex simulations. This  
407 may be explained by considering that, for large time steps, vertex positions move further than  
408 the length threshold for cell rearrangements, and instances when the lengths of cell-cell interfaces  
409 fall below this threshold may not be resolved. Importantly, in order for differences in simulation  
410 results to be negligibly small, a time step has to be chosen that is five orders of magnitude smaller  
411 than the average cell cycle duration in our simulation, and six orders of magnitude smaller than  
412 the simulation time. For individual simulations, simulation outcomes may change if a smaller  
413 time step is chosen. In our simulations, differences in simulation outcomes with decreasing  
414 time steps occurred at all observed choices of the time step. More research is required to  
415 analyse the extent to which further decreases in the time step can lead to convergence of the  
416 simulation results. Here, we stopped investigating the effects of further decreasing the time

417 step due to prohibitive increases in calculation times as the time step is decreased. In previous  
418 studies, vertex models have been reported to converge as the time step is decreased [45, 60].  
419 Our analysis differs from these previous studies by considering a tissue undergoing cell division  
420 and rearrangement rather than relaxation from an initial condition.

421 The simulation results are sensitive to the T1 transition threshold chosen in the simulation.  
422 The size of the T1 transition threshold can be used to regulate the extent to which the simulated  
423 tissue is allowed to rearrange in order to minimise energy. Literature values for this quantity  
424 span a range from 0.1 [4] to 0.01 [27]. Final vertex positions of individual simulations change  
425 with the value for the T1 transition threshold and do not converge as the threshold is decreased.

426 Our results that both the time step and the cell rearrangement threshold may influence  
427 the rate of T1 transitions illustrates that these parameters are interconnected. When the time  
428 step is chosen sufficiently large such that vertices move further than the cell rearrangement  
429 threshold between time steps, cell rearrangement is suppressed. This means that if a small cell  
430 rearrangement threshold is chosen, a sufficiently small time step needs to be chosen. A careful  
431 choice of time steps and cell rearrangement threshold is crucial since an incorrect choice may lead  
432 to failure of the simulation algorithm. For vertex models designed to simulate polycrystalline  
433 materials an adaptive time stepping scheme has been developed that resolves the exact time  
434 at which the end points of a short edge meet, and a T1 transition is performed whenever this  
435 happens [18]. More work is required to understand how rates of T1 transitions differ if different  
436 conditions for rearrangement are implemented, such as the shortening of an edge to a given  
437 threshold or the shrinking edge of an edge to a point. Ultimately, the optimal algorithm to  
438 simulate cell rearrangement in epithelial tissues can only be chosen through comparison with  
439 experimental results.

440 While simulated vertex model configurations are sensitive to the size of the time step and  
441 thresholds for cell rearrangement, they are less sensitive to the length of newly formed edges,  
442 and to thresholds for cell removal. We find that the length of newly formed edges may be up to  
443 twice as long as the threshold for T1 transitions without affecting final vertex configurations.  
444 Note that this factor by which the length of newly formed edges can be varied without affecting  
445 simulation outcomes may change in other parameter regimes, for example if larger values for  
446 the cell rearrangement threshold are chosen.

447 The size of the area threshold for cell removal may be varied over six orders of magnitude  
448 without impacting tissue level summary statistics, even though the exact number of T2 transi-  
449 tions may differ for any two values of the area threshold. In particular, it seems to be possible  
450 to choose arbitrarily small values for the T2 transition threshold without causing the algorithm  
451 to fail. There are three effects that may contribute to the stability of small elements in our  
452 simulations. (i) Since small cells with areas close to the threshold for cell removal are far away  
453 from their preferred area in our simulations ( $A_{0,\alpha} > 1.0$ ), their area force is larger than that  
454 of adjacent neighbours. This makes the cells stiff and prevents them from becoming inverted  
455 or otherwise misshapen. (ii) Additionally, the relationship between area and cell neighbour  
456 numbers number in figure 2 shows that small elements are most likely to be triangular. Our  
457 simulation algorithm does not permit T1 transitions if the short edge is part of a triangular cell  
458 in order to prevent triangular elements from becoming inverted and thus the algorithm from  
459 failure. (iii) This relationship between cell area and cell neighbour number may also contribute  
460 to the stability of the algorithm when the area threshold is large, for example 0.2. In this case,  
461 individual cells may be smaller than the area threshold without undergoing T2 transitions if  
462 they are not triangular.

463 The energy equation (2) provides a geometrical hypothesis for the removal of cells from ep-  
464 ithelia, in which cells are removed from the tissue if this is energetically favourable. Mechanical  
465 effects of cell death are an area of increasing biophysical interest [61], and it is subject of future  
466 work to design vertex models that allow alternative hypothesis for cell death to be tested.

467 Here, we analysed how non-biophysical parameters can influence experimentally measurable  
468 summary statistics in cell-based models by examining a force-propagation-based implementation  
469 of vertex models. Individual results may be relevant to other implementation choices. For  
470 example, our finding that the duration of the cell cycle in our model influences simulation  
471 outcomes may mean that parameters that control the rate of energy-minimisation may influence  
472 results in other vertex model implementations [3, 24, 62]. In general, further work is required  
473 to understand how other choices of implementation schemes may impact computational model  
474 predictions. For example, the noise strength in a Monte-Carlo vertex propagation scheme [39, 40]  
475 or the choice of energy-minimisation algorithm may influence vertex model behaviour.

## 476 **5 Conclusions**

477 Our results illustrate that care needs to be taken when drawing predictions using cell-based  
478 computational models because implementation details such as the size of the time step may  
479 influence model predictions significantly. With the rise of quantitative analysis and quantitative  
480 model-data comparison in biophysical applications, choices of model implementation become  
481 increasingly relevant. To enable the use of cell-based models in quantitative settings, it is  
482 important to be aware of any influences that implementation parameters may have on model  
483 predictions when analysing a specific biophysical phenomenon. Understanding model behaviour  
484 in detail is crucial to prevent modelling artefacts from influencing experimental predictions  
485 and clouding our biophysical understanding and, as such, our findings emphasise the need to  
486 fully document algorithms for simulating cell-based models. Close attention to implementation  
487 details is required in order to unravel the full predictive power of cell-based models.

## 488 **Acknowledgements**

489 J.K. acknowledges funding from the Engineering and Physical Sciences Research Council through  
490 a studentship. The authors would like to acknowledge the use of the University of Oxford Ad-  
491 vanced Research Computing (ARC) facility in carrying out this work.

## 492 **References**

- 493 [1] Kitano, H. Systems biology: A brief overview. *Science*, 295(5560):1662–1664, 2002. doi:  
494 10.1126/science.1069492.
- 495 [2] Fisher, J. and Henzinger, T. A. Executable cell biology. *Nature Biotechnol.*, 25(11):1239–  
496 49, 2007. doi:10.1038/nbt1356.
- 497 [3] Farhadifar, R., Röper, J.-C., Aigouy, B., Eaton, S., and Jülicher, F. The influence of  
498 cell mechanics, cell-cell interactions, and proliferation on epithelial packing. *Curr. Biol.*,  
499 17(24):2095–2104, 2007. doi:10.1016/j.cub.2007.11.049.

- 500 [4] Mao, Y., Tournier, A. L., Bates, P. A., Gale, J. E., Tapon, N., and Thompson, B. J. Planar  
501 polarization of the atypical myosin Dachs orients cell divisions in *Drosophila*. *Genes Dev.*,  
502 25(2):131–136, 2011. doi:10.1101/gad.610511.
- 503 [5] Trichas, G., Smith, A. M., White, N., Wilkins, V., Watanabe, T., Moore, A., Joyce,  
504 B., Sugnaseelan, J., Rodriguez, T. A., Kay, D., et al. Multi-cellular rosettes in the mouse  
505 visceral endoderm facilitate the ordered migration of anterior visceral endoderm cells. *PLoS*  
506 *Biol.*, 10(2):e1001256, 2012. doi:10.1371/journal.pbio.1001256.
- 507 [6] Monier, B., Gettings, M., Gay, G., Mangeat, T., Schott, S., Guarner, A., and Suzanne,  
508 M. Apico-basal forces exerted by apoptotic cells drive epithelium folding. *Nature*,  
509 518(7538):245–248, 2015. doi:10.1038/nature14152.
- 510 [7] Atwell, K., Qin, Z., Gavaghan, D., Kugler, H., Hubbard, E. J., and Osborne, J. M.  
511 Mechano-logical model of *C. elegans* germ line suggests feedback on the cell cycle. *De-*  
512 *velopment*, 142(22):3902–3911, 2015. doi:10.1242/dev.126359.
- 513 [8] Walker, D. C., Hill, G., Wood, S. M., Smallwood, R. H., and Southgate, J. Agent-based  
514 computational modeling of wounded epithelial cell monolayers. *IEEE Trans. Nanobio-*  
515 *science*, 3(3):153–163, 2004.
- 516 [9] Anderson, A. R. A., Weaver, A. M., Cummings, P. T., and Quaranta, V. Tumor morphology  
517 and phenotypic evolution driven by selective pressure from the microenvironment. *Cell*,  
518 127(5):905–915, 2006. doi:10.1016/j.cell.2006.09.042.
- 519 [10] Weinan, E. and Engquist, B. Multiscale modeling and computation. *Notices Amer. Math.*  
520 *Soc.*, 50(9):1062–1070, 2003.
- 521 [11] Miller, R. E. and Tadmor, E. B. A unified framework and performance benchmark of  
522 fourteen multiscale atomistic/continuum coupling methods. *Model. Simul. Mater. Sci.*  
523 *Eng.*, 17(5):053001, 2009. doi:10.1088/0965-0393/17/5/053001.
- 524 [12] Pantazis, P. and Supatto, W. Advances in whole-embryo imaging: a quantitative transition  
525 is underway. *Nat. Rev. Mol. Cell. Biol.*, 15(5):327–339, 2014. doi:10.1038/nrm3786.

- 526 [13] Yu, J. C. and Fernandez-Gonzalez, R. Quantitative modelling of epithelial morphogenesis:  
527 integrating cell mechanics and molecular dynamics. *Sem. Cell Dev. Biol.*, 2016. doi:10.  
528 1016/j.semcdb.2016.07.030.
- 529 [14] Pargett, M. and Umulis, D. M. Quantitative model analysis with diverse biological data:  
530 Applications in developmental pattern formation. *Methods*, 62(1):56–67, 2013. doi:10.  
531 1016/j.ymeth.2013.03.024.
- 532 [15] Fletcher, A. G., Osterfield, M., Baker, R. E., and Shvartsman, S. Y. Vertex models of  
533 epithelial morphogenesis. *Biophys. J.*, 106(11):2291–2304, 2014. doi:10.1016/j.bpj.2013.11.  
534 4498.
- 535 [16] Okuzono, T. and Kawasaki, K. Intermittent flow behavior of random foams: A computer  
536 experiment on foam rheology. *Phys. Rev. E*, 51(2):1246–1253, 1995. doi:10.1103/PhysRevE.  
537 51.1246.
- 538 [17] Kawasaki, K., Nagai, T., and Nakashima, K. Vertex models for two-dimensional grain  
539 growth. *Philos. Mag. B*, 60(3):399–421, 1989. doi:10.1080/13642818908205916.
- 540 [18] Torres, C. E., Emelianenko, M., Golovaty, D., Kinderlehrer, D., and Ta’asan, S. Numerical  
541 analysis of the vertex models for simulating grain boundary networks. *SIAM J. Appl.*  
542 *Math.*, 75(2):762–786, 2015. doi:10.1137/140999232.
- 543 [19] Honda, H. Description of cellular patterns by Dirichlet domains: The two-dimensional  
544 case. *J. Theor. Biol.*, 72(3):523–543, 1978. doi:10.1016/0022-5193(78)90315-6.
- 545 [20] Nagai, T., Kawasaki, K., and Nakamura, K. Vertex dynamics of two-dimensional cellular  
546 patterns. *J. Phys. Soc. Jpn.*, 57(7):2221–2224, 1988. doi:10.1143/JPSJ.57.2221.
- 547 [21] Weliky, M. and Oster, G. The mechanical basis of cell rearrangement. I. Epithelial mor-  
548 phogenesis during *Fundulus* epiboly. *Development*, 109(2):373–386, 1990.
- 549 [22] Nagai, T. and Honda, H. A dynamic cell model for the formation of epithelial tissues.  
550 *Philos. Mag. B*, 81(7):699–719, 2001. doi:10.1080/13642810108205772.
- 551 [23] Alberts, B., Johnson, A., Lewis, J., Raff, M., Roberts, K., and Walter, P. *Molecular Biology*  
552 *of the Cell*, 5<sup>th</sup> Ed. Garland Science, 2008.

- 553 [24] Aegerter-Wilmsen, T., Smith, A., Christen, A., Aegerter, C., Hafen, E., and Basler, K. Ex-  
554 ploring the effects of mechanical feedback on epithelial topology. *Development*, 137(3):499–  
555 506, 2010. doi:10.1242/dev.041731.
- 556 [25] Patel, A. B., Gibson, W. T., Gibson, M. C., and Nagpal, R. Modeling and inferring  
557 cleavage patterns in proliferating epithelia. *PLoS Comput. Biol.*, 5(6):e1000412, 2009.  
558 doi:10.1371/journal.pcbi.1000412.
- 559 [26] Landsberg, K. P., Farhadifar, R., Ranft, J., Umetsu, D., Widmann, T. J., Bittig, T., Said,  
560 A., Jülicher, F., and Dahmann, C. Increased cell bond tension governs cell sorting at the  
561 *Drosophila* anteroposterior compartment boundary. *Curr. Biol.*, 19(22):1950–1955, 2009.  
562 doi:10.1016/j.cub.2009.10.021.
- 563 [27] Canela-Xandri, O., Sagués, F., Casademunt, J., and Buceta, J. Dynamics and mechanical  
564 stability of the developing dorsoventral organizer of the wing imaginal disc. *PLoS Comput.*  
565 *Biol.*, 7(9):e1002153, 2011. doi:10.1371/journal.pcbi.1002153.
- 566 [28] Salbreux, G., Barthel, L. K., Raymond, P. A., and Lubensky, D. K. Coupling mechanical  
567 deformations and planar cell polarity to create regular patterns in the zebrafish retina.  
568 *PLoS Comput. Biol.*, 8(8):e1002618, 2012. doi:10.1371/journal.pcbi.1002618.
- 569 [29] Sugimura, K. and Ishihara, S. The mechanical anisotropy in a tissue promotes ordering in  
570 hexagonal cell packing. *Development*, 140(19):4091–4101, 2013. doi:10.1242/dev.094060.
- 571 [30] Kursawe, J., Brodskiy, P. A., Zartman, J. J., Baker, R. E., and Fletcher, A. G. Capabilities  
572 and limitations of tissue size control through passive mechanical forces. *PLoS Comput.*  
573 *Biol.*, 11(12):e1004679, 2015. doi:10.1371/journal.pcbi.1004679.
- 574 [31] Wartlick, O., Mumcu, P., Jülicher, F., and González-Gaitán, M. Understanding morpho-  
575 genetic growth control - lessons from flies. *Nat. Rev. Mol. Cell Biol.*, 12(9):594–604, 2011.  
576 doi:10.1038/nrm3169.
- 577 [32] Bi, D., Lopez, J. H., Schwarz, J., and Manning, M. L. Energy barriers and cell migration  
578 in densely packed tissues. *Soft Matter*, 10:1885–1890, 2014. doi:10.1039/C3SM52893F.

- 579 [33] Marinari, E., Mehonic, A., Curran, S., Gale, J., Duke, T., and Baum, B. Live-cell delamina-  
580 tion counterbalances epithelial growth to limit tissue overcrowding. *Nature*, 484(7395):542–  
581 545, 2012. doi:10.1038/nature10984.
- 582 [34] Nagai, T. and Honda, H. Computer simulation of wound closure in epithelial tissues: Cell-  
583 basal-lamina adhesion. *Phys. Rev. E*, 80:061903, 2009. doi:10.1103/PhysRevE.80.061903.
- 584 [35] Rauzi, M., Verant, P., Lecuit, T., and Lenne, P.-F. Nature and anisotropy of cortical  
585 forces orienting *Drosophila* tissue morphogenesis. *Nat. Cell Biol.*, 10(12):1401–1410, 2008.  
586 doi:10.1038/ncb1798.
- 587 [36] Collinet, C., Rauzi, M., Lenne, P.-F., and Lecuit, T. Local and tissue-scale forces drive  
588 oriented junction growth during tissue extension. *Nat. Cell Biol.*, 17(10):1247–1258, 2015.  
589 doi:10.1038/ncb3226.
- 590 [37] Tetley, R. J., Blanchard, G. B., Fletcher, A. G., Adams, R. J., and Sanson, B. Unipolar dis-  
591 tributions of junctional myosin ii identify cell stripe boundaries that drive cell intercalation  
592 throughout *Drosophila* axis extension. *eLife*, 5:1–35, 2016. doi:10.7554/eLife.12094.
- 593 [38] Mao, Y., Tournier, A. L., Hoppe, A., Kester, L., Thompson, B. J., and Tapon, N. Differ-  
594 ential proliferation rates generate patterns of mechanical tension that orient tissue growth.  
595 *EMBO J.*, 32(21):2790–2803, 2013. doi:10.1038/emboj.2013.197.
- 596 [39] Etournay, R., Popovi, M., Merkel, M., Nandi, A., Blasse, C., Aigouy, B., Brandl, H., Myers,  
597 G., Salbreux, G., Jlicher, F., et al. Interplay of cell dynamics and epithelial tension during  
598 morphogenesis of the *Drosophila* pupal wing. *eLife*, 4:e07090, 2015. doi:10.7554/eLife.  
599 07090.
- 600 [40] Ray, R. P., Matamoro-Vidal, A., Ribeiro, P. S., Tapon, N., Houle, D., Salazar-Ciudad,  
601 I., and Thompson, B. J. Patterned anchorage to the apical extracellular matrix defines  
602 tissue shape in the developing appendages of *Drosophila*. *Dev. Cell*, 34(3):310–322, 2015.  
603 doi:10.1016/j.devcel.2015.06.019.
- 604 [41] Staple, D., Farhadifar, R., Röper, J.-C., Aigouy, B., Eaton, S., and Jülicher, F. Mechanics  
605 and remodelling of cell packings in epithelia. *Eur. Phys. J. E*, 33:117–127, 2010. doi:  
606 10.1140/epje/i2010-10677-0.

- 607 [42] Merzouki, A., Malaspinas, O., and Chopard, B. The mechanical properties of a cell-  
608 based numerical model of epithelium. *Soft Matter*, 12(21):4745–4754, 2016. doi:10.1039/  
609 C6SM00106H.
- 610 [43] Xu, G.-K., Liu, Y., and Li, B. How do changes at the cell level affect the mechanical  
611 properties of epithelial monolayers? *Soft Matter*, 11(45):8782–8788, 2015. doi:10.1039/  
612 C5SM01966D.
- 613 [44] Davit, Y., Osborne, J., Byrne, H., Gavaghan, D., and Pitt-Francis, J. Validity of the  
614 cauchy-born rule applied to discrete cellular-scale models of biological tissues. *Phys. Rev.*  
615 *E*, 87(4):042724, 2013. doi:10.1103/PhysRevE.87.042724.
- 616 [45] Smith, A. M., Baker, R. E., Kay, D., and Maini, P. K. Incorporating chemical signalling  
617 factors into cell-based models of growing epithelial tissues. *J. Math. Biol.*, 65:441–463,  
618 2012. doi:10.1007/s00285-011-0464-y.
- 619 [46] Osborne, J. M., Fletcher, A. G., Pitt-Francis, J. M., Maini, P. K., and Gavaghan, D. J.  
620 Comparing individual-based approaches to modelling the self-organization of multicellular  
621 tissues. *bioRxiv*, 2016. doi:10.1101/074351.
- 622 [47] Magno, R., Grieneisen, V. A., and Marée, A. F. M. The biophysical nature of cells:  
623 potential cell behaviours revealed by analytical and computational studies of cell surface  
624 mechanics. *BMC Biophys.*, 8(1):8, 2015. doi:10.1186/s13628-015-0022-x.
- 625 [48] Fletcher, A. G., Osborne, J. M., Maini, P. K., and Gavaghan, D. J. Implementing vertex dy-  
626 namics models of cell populations in biology within a consistent computational framework.  
627 *Prog. Biophys. Mol. Biol.*, 113(2):299–326, 2013. doi:10.1016/j.pbiomolbio.2013.09.003.
- 628 [49] Mirams, G. R., Arthurs, C. J., Bernabeu, M. O., Bordas, R., Cooper, J., Corrias, A.,  
629 Davit, Y., Dunn, S.-J., Fletcher, A. G., Harvey, D. G., et al. Chaste: An open source C++  
630 library for computational physiology and biology. *PLoS Comput. Biol.*, 9(3):e1002970,  
631 2013. doi:10.1371/journal.pcbi.1002970.
- 632 [50] Smith, J. A. and Martin, L. Do cells cycle? *Proc. Natl. Acad. Sci. USA*, 70(4):1263–1267,  
633 1973. doi:10.1073/pnas.70.4.1263.

- 634 [51] Shields, R. Further evidence for a random transition in the cell cycle. *Nature*, 273:755–758,  
635 1978. doi:10.1038/273755a0.
- 636 [52] Hofmeister, W. Zusätze und Berichtigungen zu den 1851 veröffentlichten Untersuchungen  
637 der Entwicklung höherer Kryptogamen. *Jahrb. wiss. Bot.*, 3:259–293, 1863.
- 638 [53] Gibson, W. T., Veldhuis, J. H., Rubinstein, B., Cartwright, H. N., Perrimon, N., Brodland,  
639 G. W., Nagpal, R., and Gibson, M. C. Control of the mitotic cleavage plane by local  
640 epithelial topology. *Cell*, 144(3):427–438, 2011. doi:10.1016/j.cell.2010.12.035.
- 641 [54] Lewis, F. T. The correlation between cell division and the shapes and sizes of prismatic cells  
642 in the epidermis of cucumis. *Anat. Rec.*, 38(3):341–376, 1928. doi:10.1002/ar.1090380305.
- 643 [55] Kim, S., Cai, M., and Hilgenfeldt, S. Lewis’ law revisited: the role of anisotropy in  
644 sizetopology correlations. *New J. Phys.*, 16(1):015024, 2014. doi:10.1088/1367-2630/16/1/  
645 015024.
- 646 [56] Milán, M., Campuzano, S., and García-Bellido, A. Cell cycling and patterned cell prolif-  
647 eration in the wing primordium of *Drosophila*. *Proc. Natl. Acad. Sci. USA*, 93:640–645,  
648 1996. doi:10.1073/pnas.93.2.640.
- 649 [57] Ishihara, S. and Sugimura, K. Bayesian inference of force dynamics during morphogenesis.  
650 *J. Theor. Biol.*, 313(0):201–211, 2012. doi:10.1016/j.jtbi.2012.08.017.
- 651 [58] Ishihara, S., Sugimura, K., Cox, S., Bonnet, I., Bellaïche, Y., and Graner, F. Comparative  
652 study of non-invasive force and stress inference methods in tissue. *Eur. Phys. J. E*, 36(4):1–  
653 13, 2013. doi:10.1140/epje/i2013-13045-8.
- 654 [59] Chiou, K. K., Hufnagel, L., and Shraiman, B. I. Mechanical stress inference for two-  
655 dimensional cell arrays. *PLoS Comput. Biol.*, 8(5):e1002512, 2012. doi:10.1371/journal.  
656 pcbi.1002512.
- 657 [60] Smith, A. M. Vertex model approaches to epithelial tissues in developmental systems.  
658 Ph.D. thesis, University of Oxford, 2011.
- 659 [61] Ambrosini, A., Gracia, M., Proag, A., Rayer, M., Monier, B., and Suzanne, M. Apoptotic  
660 forces in tissue morphogenesis. *Mech. Dev.*, 2016. doi:10.1016/j.mod.2016.10.001.

661 [62] Aegerter-Wilmsen, T., Heimlicher, M., Smith, A., de Reuille, P., Smith, R., Aegerter,  
662 C., and Basler, K. Integrating force-sensing and signaling pathways in a model for the  
663 regulation of wing imaginal disc size. *Development*, 139(17):3221–3231, 2012. doi:10.1242/  
664 dev.082800.